marine drugs

MDPI

Article

Synthesis, Biological Evaluation, and Computational Studies of Phenolic *N*-Acetylglucosamine Glycosides as α-Glucosidase Inhibitors

Wenjie Wang [1,2,†], Kun Gao [1,†], Guantian Li [1], Zongji Wang [3], Kecheng Li [1,4], Song Liu [1,4], Huahua Yu [1,4] and Ronge Xing [1,4,*]

[1] Laboratory of Experimental Marine Biology, Institute of Oceanology, Chinese Academy of Sciences, Qingdao 266000, China
[2] University of Chinese Academy of Sciences, Beijing 100049, China
[3] Regenerative Medicine Innovation Institute, Linyi University, Linyi 276012, China
[4] Laboratory for Marine Drugs and Bioproducts, Qingdao Marine Science and Technology Center, Qingdao 266237, China
* Correspondence: xingronge@qdio.ac.cn; Tel.: +86-532-8289-8780
† These authors contributed equally to this work.

Abstract

Type 2 diabetes mellitus (T2DM) is one of the most prevalent chronic metabolic diseases, and inhibition of α-glucosidase activity represents an effective therapeutic strategy. Chitin is the most abundant renewable polysaccharide in the ocean, with its monosaccharide being *N*-acetylglucosamine (NAG). To evaluate the potential of NAG glycosides as novel α-glucosidase inhibitors, three common phenolic compounds were modified via NAG glycosylation. Their inhibitory activities were assessed at both the enzymatic and cellular levels. In addition, density functional theory (DFT), molecular dynamics (MD) simulations, and molecular docking analyses were employed to systematically investigate the effects of NAG glycosylation on enzyme inhibition and the underlying mechanisms. Compared with the parent phenolic compounds, NAG glycosides exhibited significantly enhanced α-glucosidase inhibitory activity, with NAG introduction markedly improving their binding affinity to α-glucosidase. Among them, glycoside **3a** displayed the optimal inhibitory effect, comparable to acarbose, and at the cellular level, its activity at high concentrations was comparable to or slightly higher than that of metformin. Circular dichroism (CD) and MD analyses indicated that glycoside **3a** increased the conformational flexibility of key residues and enhanced the structural looseness of the enzyme, thereby inhibiting its activity. NAG glycosides constitute a promising class of marine-derived α-glucosidase inhibitors, warranting further structural optimization and rational design to enhance their activity and selectivity.

Keywords: α-glucosidase inhibitor; *N*-acetylglucosamine glycoside; phenols; DFT; molecular dynamic; diabetes

Check for updates

Academic Editors: Yuki Fujii, Marco Gerdol, Ogawa Yukiko and Yasuhiro Ozeki

Received: 30 January 2026
Revised: 13 February 2026
Accepted: 17 February 2026
Published: 19 February 2026

Copyright: © 2026 by the authors. Licensee MDPI, Basel, Switzerland. This article is an open access article distributed under the terms and conditions of the Creative Commons Attribution (CC BY) license.

1. Introduction

Diabetes mellitus (DM) is a chronic metabolic disorder characterized by persistent hyperglycemia [1]. T2DM accounts for more than 90% of all DM cases and is mainly associated with insufficient insulin secretion and peripheral insulin resistance [2]. Sustained hyperglycemia not only causes direct tissue damage but also leads to severe complications affecting the eyes, kidneys, heart, nerves, and blood vessels, thereby greatly increasing

morbidity and mortality [3,4]. Controlling postprandial blood glucose (PBG) has been recognized as a key therapeutic strategy for T2DM. α-Glucosidase, a hydrolase located in the brush border of the small intestine, catalyzes the breakdown of oligosaccharides and disaccharides into glucose and thus regulates the absorption rate of carbohydrates [5,6]. Inhibiting α-glucosidase delays carbohydrate digestion, lowers PBG levels, and is an effective strategy for T2DM management. Currently available α-glucosidase inhibitors, including acarbose, voglibose, and miglitol, are clinically applied but often cause gastrointestinal side effects such as bloating and diarrhea, limiting long-term patient compliance [7]. Therefore, the development of safer and more effective α-glucosidase inhibitors remains highly desirable.

Natural products have long been regarded as highly valuable sources for drug discovery [8]. Glycosides represent an important class of natural products, including phenolic, triterpenoid, and flavonoid glycosides, and have been reported to exhibit a broad range of pharmacological activities such as anti-inflammatory, antibacterial, antioxidant, and hypoglycemic effects [9–11]. Notably, an increasing number of studies have demonstrated that several natural glycosides show significant α-glucosidase inhibitory activity and are capable of lowering blood glucose levels in diabetic animal models, indicating their potential relevance for antidiabetic drug development (Figure 1) [12–16]. For example, compound **I** isolated from Trollius chinensis Bunge by Feng et al. displayed an IC_{50} value of 3.14 μM against α-glucosidase [12]. Li et al. also identified multiple glucose-based glycosides from *Viburnum chinshanense* leaves with strong inhibitory activity [13]. However, these highly active glycosides often possess structurally complex scaffolds and require lengthy synthetic pathways, which hampers large-scale preparation and practical development [17,18]. Moreover, most of these enzyme-inhibitory glycosides contain a glucose moiety that is readily hydrolyzed in vivo, releasing free glucose and potentially elevating blood glucose levels [19,20]. This metabolic behavior restricts their modes of administration and may limit the full realization of their therapeutic potential. This situation calls for innovative glycoside design strategies that avoid glucose-derived liabilities while maintaining or enhancing inhibitory potency.

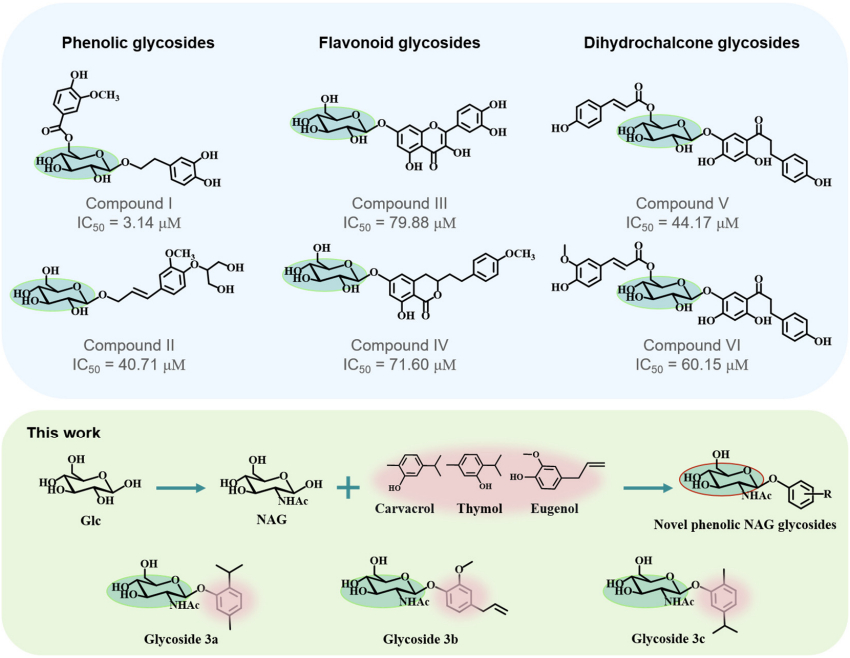


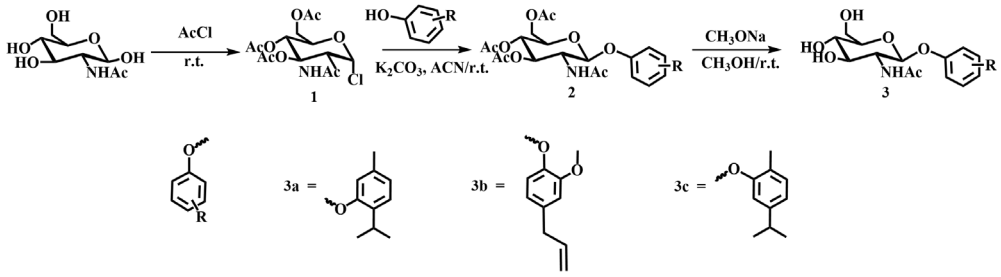
Figure 1. Structures of previously reported high-activity glucosides and the design strategy of phenolic NAG glycosides.

Replacing glucose with other monosaccharides or sugar analogues is a common strategy for designing α glucosidase inhibitors [21]. However, the use of NAG as the sugar moiety in such inhibitors has been rarely reported. NAG is the fundamental structural unit of chitin, the most abundant polysaccharide in the oceans and the Earth's most plentiful nitrogen-containing biomass resource. It has garnered significant attention due to its safety, non-toxicity, green and renewable properties, and broad biological activity [22]. Accumulating studies have reported that NAG, as a functional monosaccharide, exhibits a range of biological activities, including antibacterial, antioxidant, antiviral, antitumor, and anti-inflammatory effects [23]. In the present study, NAG was employed as the sugar moiety and glycosylated with several structurally simple phenolic compounds previously reported to exhibit α glucosidase inhibitory activity (Figure 1). The in vitro enzyme inhibitory activities of the resulting NAG glycoside conjugates were compared with those of the corresponding aglycones. Furthermore, DFT, molecular docking, and MD simulations were conducted to investigate the role of glycosylation and the inhibitory mechanism of the NAG glycosides, providing a comprehensive evaluation of their potential as novel high activity α glucosidase inhibitor scaffolds. This work is expected to offer new insights for the design of glycosidic α glucosidase inhibitors and to facilitate the discovery of safe and effective lead compounds for diabetes therapy from marine sources.

2. Results

2.1. Chemistry

The synthetic route for natural phenolic NAG glycosides is illustrated in Scheme 1. During the reaction of acetyl chloride with NAG, the C1-hydroxyl group undergoes initial acylation with the concomitant release of hydrogen chloride. Under acid catalysis, the C2-acetamido group attacks the C1 position via the neighboring group participation effect, displacing the leaving group to form a cyclic oxazolinium intermediate. Subsequently, the chloride ion in the system nucleophilically attacks the C1 position of this intermediate, ultimately yielding the glycosyl chloride donor **1**. Subsequently, under basic conditions using potassium carbonate as an acid scavenger, the chloride undergoes nucleophilic substitution with various phenolic hydroxyl groups, yielding fully acetyl-protected phenolic NAG glycosides. Notably, compound **1** lacks ultraviolet absorption at 254 nm, allowing for the rapid collection of the more polar glycosylation product **2** via TLC-based monitoring and preparative separation. The acetyl protecting groups on the sugar ring of intermediate **2** are then efficiently removed using a methanol/sodium methoxide solution, affording the final product, glycoside **3**. This deprotection step proceeds with near-quantitative conversion and does not require silica gel column chromatography; instead, the product can be readily purified by recrystallization. The structure of glycoside **3** was confirmed by NMR, HRMS and IR (Figures S1–S10). For example, in the ^{1}H NMR spectrum of glycoside **3a**, in addition to the signals attributable to the sugar ring protons, a characteristic resonance at $\delta \approx 7.0$ ppm corresponding to three aromatic protons was observed. Moreover, signals at $\delta \approx 1.0$ ppm were assigned to two methyl groups, with an integral value of approximately six protons, consistent with the presence of two equivalent methyl substituents. In the ^{13}C NMR spectrum, the characteristic signals of the aromatic carbons and the methyl carbons attached to the aromatic ring were clearly detected, and all observed resonances were in agreement with the proposed structure. Collectively, these NMR data support the structural assignment of glycoside **3a**. This synthetic strategy offers a highly efficient, low-energy, and scalable approach for the preparation of phenolic NAG glycosides, making it well-suited for industrial application.



Scheme 1. The synthetic route of the phenol glycosides.

2.2. α-Glucosidase Inhibitory Activity

The α-glucosidase inhibitory activities of all synthesized NAG glycosides and their corresponding phenolic aglycones were evaluated at multiple concentrations, with acarbose serving as the positive control (Figure 2). In general, the glycosides exhibited markedly stronger inhibitory effects than their respective aglycones. For example, at 800 μM, thymol showed an inhibition rate of only 14.44%, whereas its NAG glycosyl conjugate **3a** reached 90.09%, indicating a substantial activity enhancement upon glycosylation. Consistent with this trend, glycoside **3a** displayed an IC_{50} value of 265.8 ± 13.0 μM, which is slightly lower than that of acarbose (298.5 ± 13.7 μM). Its α-glucosidase inhibitory activity is on par with that of most previously reported glucosyl glycosides [13,24,25]. Collectively, these findings highlight the excellent enzymatic inhibitory profile of glycoside **3a** and suggest that NAG glycosides may represent a promising new structural class of α-glucosidase inhibitors.

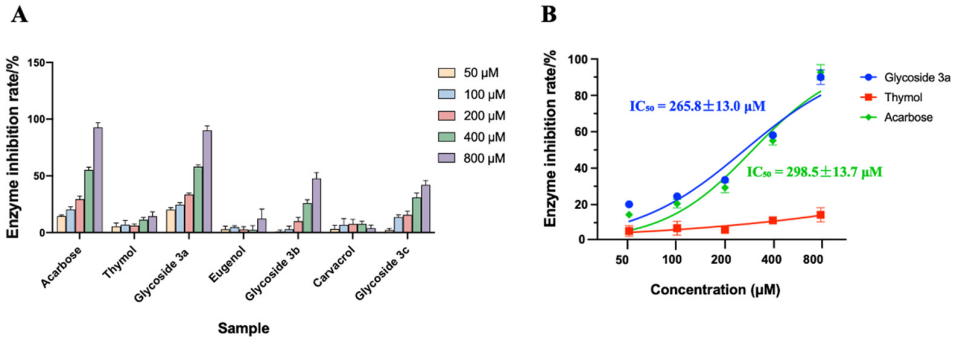


Figure 2. Enzyme inhibitory activity of glycoside **3** against α-glucosidase. (**A**) Effects of different concentrations of glycoside **3a–c** on the enzyme activity of α-glucosidase. (**B**) The half-maximal inhibitory concentration (IC_{50}) of glycoside **3a** against α-glucosidase.

2.3. Computational Study of Glycosylation-Induced Modulation of Activity

2.3.1. DFT Studies

According to the enzymatic inhibition assays, NAG glycosylation markedly enhanced the inhibitory potency of phenolic scaffolds, although the glycosides derived from different phenols displayed distinct activity levels. Due to the limited number of derivatives, a statistically robust quantitative structure–activity relationship model could not be established; therefore, DFT calculations were conducted to rationalize, from an electronic-structure perspective, how glycosylation modulates the behavior of different aglycones and contributes to the observed activity trend. The quantum-chemical outputs and corresponding visual representations are provided in Figure 3 and Table 1. The relative energy (E′) analysis revealed that all three glycosides became less stable after conjugation, whereas glycoside **3a** showed the smallest energy increase, suggesting milder electronic and conformational perturbation between NAG and its aglycone, thymol. This observation was consistent with the dipole moment values: NAG exhibits a dipole moment of 5.650253 Debye, and glycoside **3a** retains a comparable value of 5.579567 Debye. In contrast, glycoside **3b** and

glycoside **3c** showed markedly reduced dipole moments (4.870010 and 3.798859 Debye), indicative of more extensive charge redistribution across the sugar–aglycone interface. The molecular electrostatic potential (MEP) maps provided further insight. Glycoside **3c** exhibited an additional electron-deficient region (blue region) around the C6–OH position of the sugar ring, disrupting the native polarity pattern of NAG and giving rise to a substantially lower dipole moment. A diminished dipole generally denotes decreased polarity and weaker hydration, which is in line with the experimental observation that glycoside **3c** exhibits poorer aqueous solubility than glycoside **3a**, likely compromising its ability to form productive interactions with the enzyme.

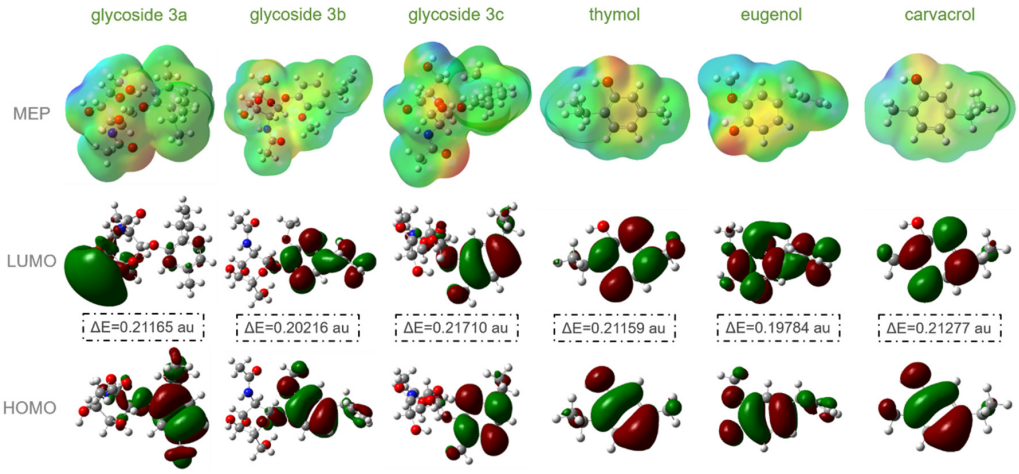


Figure 3. Electrostatic potential diagrams: HOMO and LUMO visualizations of glycosides and phenols.

Table 1. Physicochemical properties of glycosides and phenols calculated based on the B3LYP/6-311+g(d,p) basis set.

Compound	Etotal/Hartree	Dipole/Debye	Polarization/a.u.	E′/Hartree
glycoside **3a**	−1208.628867	5.579567	242.554703	0.001299
glycoside **3b**	−1282.619724	4.870010	252.255326	0.008845
glycoside **3c**	−1208.627963	3.798859	242.579667	0.005911
thymol	−464.857438	1.576435	123.239934	-
eugenol	−538.855841	2.942245	129.557667	-
carvacrol	−464.861146	1.488219	123.250333	-
NAG	−820.231191	5.650253	124.822667	

$E' = E_{total} - E_{NAG} + E_{H2O} - E_{phenols}$.

Frontier molecular orbital (FMO) analysis further clarified the electronic basis for the enhanced activity of glycoside **3a**. While the highest occupied molecular orbital (HOMO) and lowest unoccupied molecular orbital (LUMO) of the parent phenols, as well as those of glycoside **3b** and glycoside **3c**, remained primarily localized on the aglycone, glycoside **3a** showed a pronounced LUMO shift from the aglycone to the C6–OH region of the sugar. This redistribution introduces an additional electron-accepting site within the sugar moiety, potentially enabling alternative polar or hydrogen-bonding interactions in the enzyme active site. Consistently, glycoside **3a** displayed a significantly narrower energy gap (0.21165 a.u.) than glycoside **3c** (0.21710 a.u.), indicating greater electronic softness and an increased propensity for charge redistribution or induced polarization in a polar enzymatic microenvironment. Taken together with the MEP and dipole moment analyses, these results suggest that glycoside **3a** benefits from more favorable electronic complementarity and interaction potential within the active site, which is likely to contribute to its superior inhibitory activity compared with the other glycosylated derivatives.

2.3.2. Molecular Docking

Building on the quantum-chemical analysis, which highlighted the electronic advantages of glycosylation and provided a plausible explanation for the superior activity of glycoside **3a**, we further investigated the enzyme–ligand interactions through molecular docking. Based on the co-crystal binding modes of the natural substrate and acarbose, the substrate-binding region and catalytic site of the α-glucosidase were first delineated. We then compared the binding patterns of the phenolic aglycones and their corresponding glycosides. As shown in Figure 4A, eugenol failed to occupy the catalytic site, whereas thymol and carvacrol were both able to bind within this region. Notably, their glycosylated derivatives adopted binding poses that closely overlapped with those of the aglycones, but exhibited markedly enhanced binding affinities. For instance, thymol bound to the α-glucosidase with an energy of −6.6 kcal/mol, while glycoside **3a** showed a significantly stronger interaction of −8.3 kcal/mol (as shown in Table S1). Analysis of the interaction profiles revealed that thymol formed only two hydrogen bonds with Arg212 and Arg214, whereas glycoside **3a** was able to establish four hydrogen bonds via its sugar moiety with Phe157, His279, Glu304, and Arg312, underscoring the crucial contribution of the sugar unit to polar contacts (Figure 4B). Moreover, comparison with acarbose indicated that although acarbose forms up to 13 hydrogen bonds and additional hydrophobic contacts, its binding energy (−8.6 kcal/mol) is comparable to that of glycoside **3a**. This observation suggests that glycosylation substantially enhances binding stability while preserving the positional role of the aglycone within the catalytic pocket.

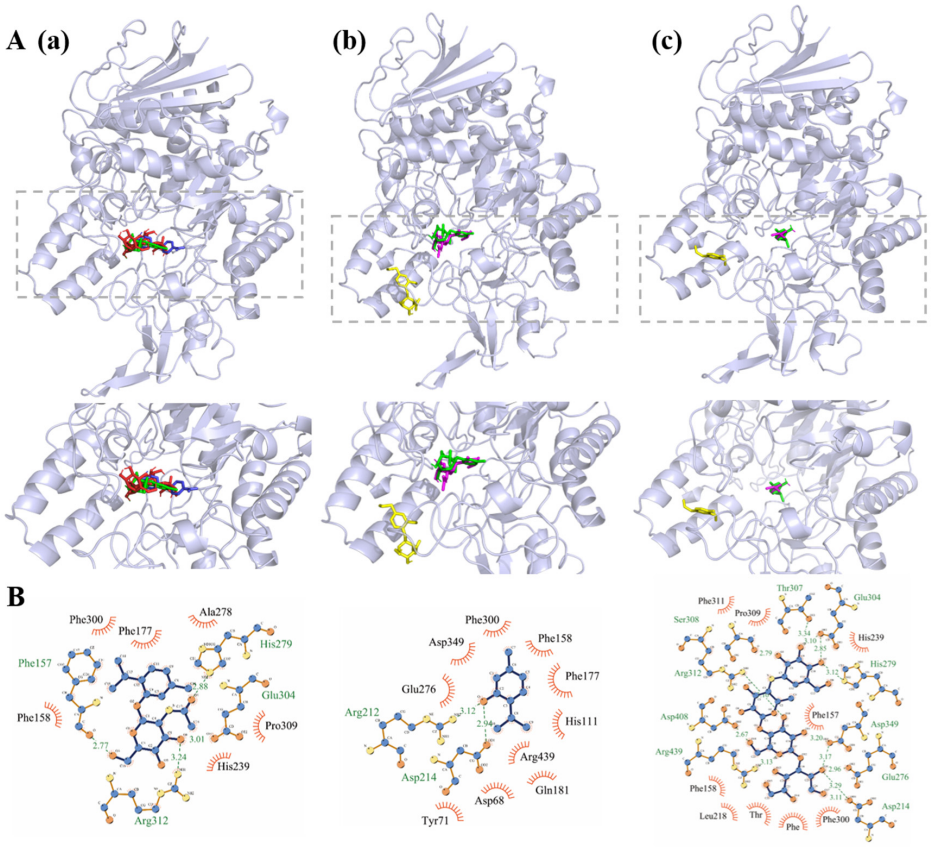


Figure 4. Molecular docking analysis of the glycosides and their corresponding phenols. (**A**) Binding modes of α-glucosidase with selected ligands: (**a**) glycoside **3a** (green), acarbose (red), and α-pNPG (blue); (**b**) glycosides **3a** (green), **3b** (yellow), and **3c** (purple); (**c**) thymol (green), eugenol (yellow), and carvacrol (purple). (**B**) Two-dimensional interaction diagrams of α-glucosidase with glycoside **3a**, thymol, and acarbose.

2.4. Mechanism of Enzyme Inhibition by Glycoside **3a**

Having elucidated the electronic features and binding behavior associated with glycosylation, we next sought to validate the inhibitory mechanism of the glycoside at the experimental level. Accordingly, inhibition kinetics and CD analyses were performed to characterize the inhibition mode of glycoside **3a** and its potential impact on the conformational state of α-glucosidase.

2.4.1. Inhibition Kinetics

Enzyme inhibitors are generally classified into competitive, noncompetitive, uncompetitive, and mixed types, which can be distinguished using the Lineweaver–Burk equation [26]. To elucidate the inhibition mode of glycoside **3a** against α-glucosidase, its inhibitory activity was assessed at varying substrate concentrations, and the corresponding Lineweaver–Burk plot was constructed (Figure 5A,B, Table 2). As the substrate concentration increased, Vmax decreased while Km increased. The reciprocal plots intersected in the second quadrant, indicating that glycoside **3a** acts as a mixed-type inhibitor of α-glucosidase [27].

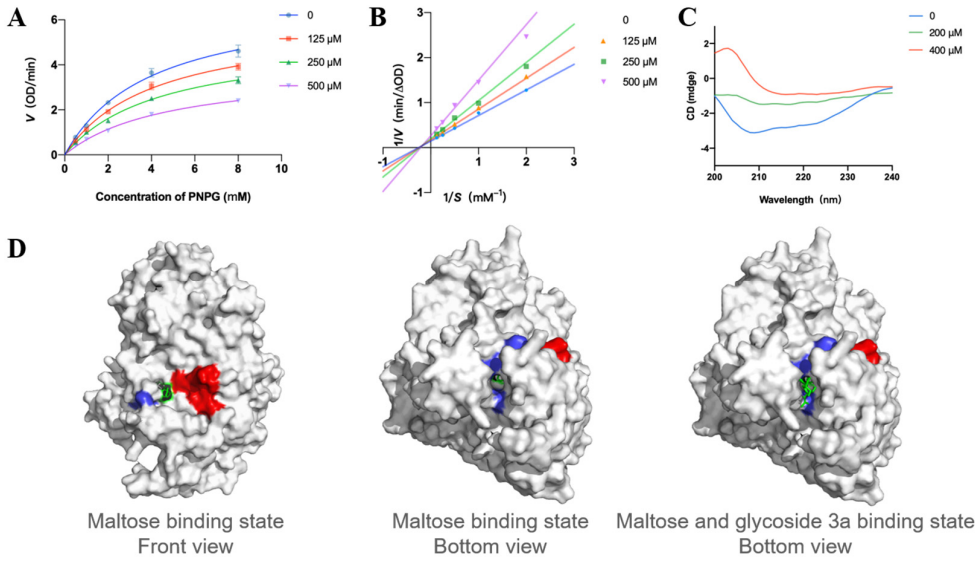


Figure 5. (**A**) Reaction rates of α-glucosidase-catalyzed substrates at different concentrations of substrate and glycoside **3a**. (**B**) The Lineweaver-Burk double reciprocal plot of the kinetics of α-glucosidase inhibition at different concentrations of substrate and glycoside **3a**. (**C**) CD spectra of α-glucosidase with glycoside **3a**. (**D**) Docking results of the α-glucosidase–maltose complex and glycoside **3a** bound to the α-glucosidase–maltose complex. The red region indicates the substrate-entry pathway, while the blue region denotes the product-release channel.

Table 2. The Michaelis constant for the α-glucosidase reaction.

Substrate	0	125 μM	250 μM	250 μM
Vmax	7.008	6.002	5.152	3.847
Km	3.991	4.124	4.378	4.760

To assess whether glycoside **3a** can bind simultaneously with the enzyme–substrate complex and thereby support its mixed-type inhibition profile, an additional set of molecular docking studies was performed. A maltose–α-glucosidase complex was first generated through docking, after which glycoside **3a** was docked into this pre-formed complex. As shown in Figure 5D, glycoside **3a** could still bind stably to the α-glucosidase even when the active site was occupied by maltose, exhibiting a binding energy of –7.1 kcal/mol. The

compound localized within the product-release channel, with the red and blue regions in Figure 5D corresponding to the substrate entry pathway and the product-release channel, respectively. These findings indicate that glycoside **3a** is capable of binding both at the catalytic site and within the product-release channel, consistent with the characteristics of a mixed-type inhibitor.

2.4.2. Circular Dichroism Spectra

CD spectroscopy is a widely used technique for analyzing protein secondary structure [28]. As could be seen from Figure 5C, α-glucosidase displays two characteristic negative peaks at 208 and 222 nm, which are indicative of α-helical structures [29]. In general, higher α-helical content correlates with greater protein stability. Upon increasing concentrations of glycoside **3a**, the intensity of these peaks progressively decreased. Quantitative analysis (Table 3) revealed that the α-helical content declined from 43.2% to 22.1% with the concentrations of glycoside **3a** increased from 0 to 400 μM, accompanied by increases in β-sheet, β-turn, and random coil content. These results suggest that glycoside **3a** disrupts the secondary structure of α-glucosidase, thereby impairing its enzymatic activity.

Table 3. The secondary structures contents of α-glucosidase.

Glycoside 3a (μM)	α-Helix (%)	β-Sheet (%)	β-Turn (%)	Random Coli (%)
0	43.2	11.9	17.9	26.5
200	36.2	18.8	18.1	27

2.5. Molecular Dynamic

To further investigate the dynamic structural changes in the α-glucosidase–glycoside **3a** complex, MD simulations were performed. Based on the most stable binding conformation of glycoside **3a** obtained from molecular docking, 150 ns MD simulations were performed for both the **3a**-bound complex and the unbound (apo) α-glucosidase. Root mean square deviation (RMSD) was employed to evaluate the structural deviations of the simulated systems over time relative to their initial conformations. Backbone RMSD analysis was first performed to assess the stability of the protein and the complex [30,31]. As shown in Figure 6A, both systems reached equilibrium around 25 ns. During the final 100 ns of the simulation, the average RMSD values for the protein and the glycoside-bound complex were approximately 0.04 nm and 0.11 nm, respectively, indicating stable conformations. The RMSD of glycoside **3a** within the binding site was also monitored. Its trend closely mirrored that of the complex, with an average RMSD of 0.09 nm in the last 100 ns, further supporting the structural stability of the ligand–protein complex (Figure S11A). In addition, the number of hydrogen bonds formed between glycoside **3a** and α-glucosidase was analyzed throughout the trajectory. As shown in Figure 6B, the number of hydrogen bonds fluctuated between 1 and 4 during the final 100 ns, consistent with the molecular docking results. This observation further confirms that the complex system had reached a stable equilibrium state.

Backbone fluctuations of amino acid residues play a crucial role in determining the dynamic stability of protein–ligand complexes [32]. The root mean square fluctuation (RMSF) is a key metric for evaluating the flexibility of individual residues and is commonly used to assess the local stability of protein systems [33]. To examine residue-level dynamics, RMSF values were calculated for both the unbound α-glucosidase protein and the α-glucosidase–glycoside **3a** complex (Figure 6C,D). In the absence of glycoside **3a**, two regions of α-glucosidase (residues 220–250 and 400–450) exhibited relatively high RMSF values. These regions correspond to loop and α-helical segments flanking the active pocket, suggesting increased flexibility near the catalytic center, which may be functionally relevant.

Upon binding of glycoside **3a**, the RMSF values of residues within the active site were notably altered, indicating that the ligand directly influences the local dynamics of these regions through specific interactions. Among the residues in the binding site, His279 displayed the most significant change in RMSF upon ligand binding. Structural analysis revealed that the imidazole ring of His279 forms a strong hydrogen bond with glycoside **3a**, which increases its conformational flexibility during the simulation.

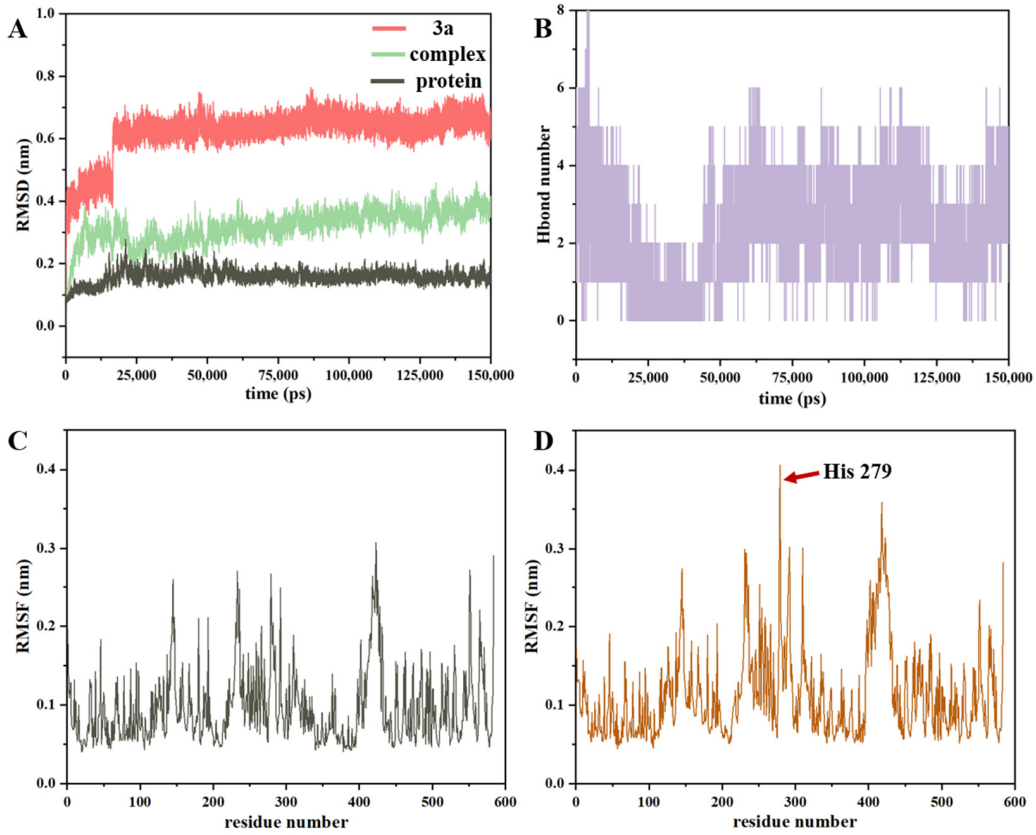


Figure 6. (**A**) The RMSD curves of the glycoside-bound complex (green line), unbound α-glucosidase (black line) and glycoside **3a** (red line). (**B**) The number of hydrogen bonds between α-glucosidase and glycoside **3a** in complex. The RMSF curve of the unbound α-glucosidase (**C**) and the glycoside-bound complex (**D**).

The radius of gyration (Rg) is a critical parameter used to evaluate the compactness and conformational stability of biomolecular structures [34]. Lower Rg values reflect a more compact and folded molecular conformation, whereas higher Rg values suggest an extended or less ordered structure. In this study, the Rg values of both the apo α-glucosidase and the α-glucosidase–glycoside **3a** complex were calculated. As shown in Figure 6C, the Rg value of the glycoside-bound complex is consistently higher than that of the unbound protein. This observation suggests that binding of glycoside **3a** induces a slight loosening or expansion of the protein structure. This conformational change is consistent with the increased flexibility observed in the RMSF analysis, indicating that glycoside **3a** binding affects the overall structural dynamics of α-glucosidase.

The solvent-accessible surface area (SASA) of a protein reflects the extent of its surface that is exposed to solvent molecules in solution [35]. A comparison of Figure 7A,B reveals that the SASA value of the α-glucosidase–glycoside **3a** complex is higher than that of the unbound protein. This result can also be obtained from Figure S11B. This increase in SASA suggests that the binding of glycoside **3a** induces a conformational change in α-glucosidase,

leading to an expansion of the binding pocket and greater exposure of surface residues to the solvent.

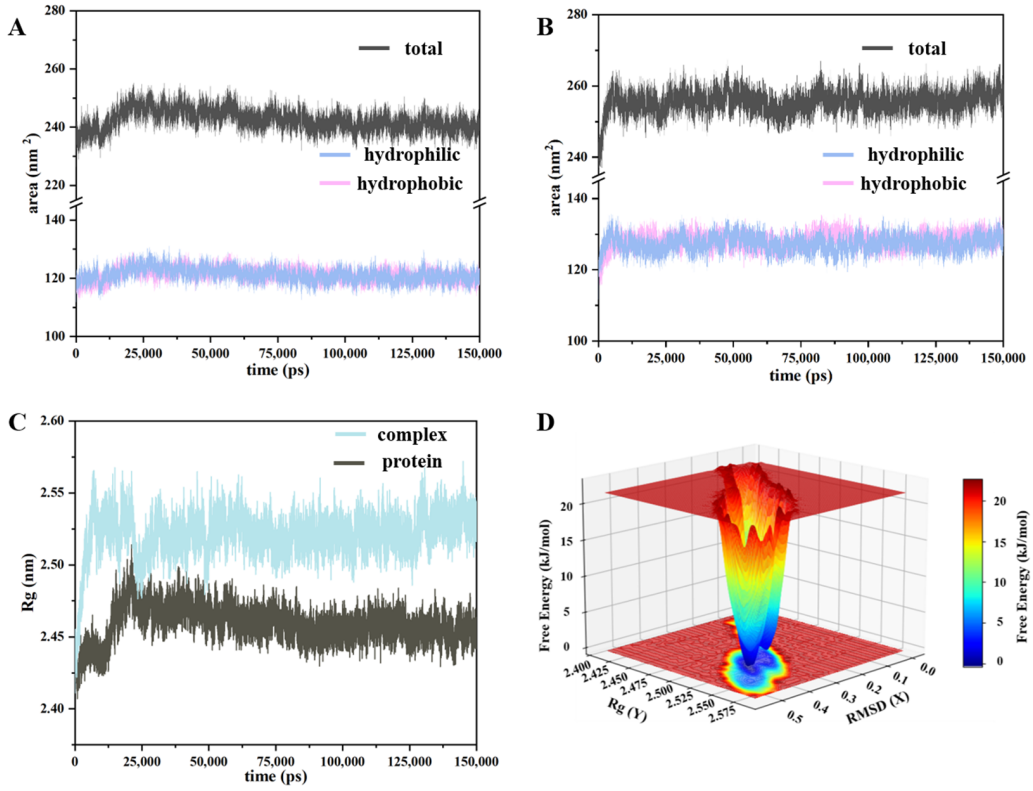


Figure 7. The SASA curves of unbound α-glucosidase (**A**) and the glycoside-bound complex (**B**). (**C**) The Rg curves of unbound α-glucosidase (black line) and the glycoside-bound complex (blue line). (**D**) The 3d FEL of the glycoside-bound complex.

Free energy landscapes (FELs) are powerful tools for visualizing conformational energy changes in proteins during MD simulations [36,37]. To explore how small-molecule binding influences the conformational energetics of the protein, FELs were constructed using radius of Rg and RMSD as reaction coordinates derived from the simulation trajectories. As shown in Figure 7D, the darker (blue) regions correspond to lower-energy conformational states, indicating enhanced structural stability. Upon binding with glycoside **3a**, α-glucosidase exhibits two distinct low-energy basins with only a minor energy difference between them. This suggests that the complex transitions dynamically between these two conformational states throughout the simulation, reflecting increased structural flexibility and dynamic fluctuations.

2.6. In Vitro Biological Evaluation Using Cellular Models

2.6.1. Evaluation of Glycoside **3a** in HepG2 Insulin-Resistant Cells

The insulin-resistant HepG2 (IR-HepG2) model is a well-established in vitro system for evaluating potential therapeutics for type 2 diabetes. In the present study, an IR-HepG2 model was successfully established to assess the ability of glycoside **3a** to ameliorate insulin resistance. As shown in Figure 8A, glucose consumption was markedly reduced in the IR group compared with the normal control (NC) group ($p < 0.01$), confirming the successful establishment of the model. Treatment with glycoside **3a** at 125, 250, and 500 μM significantly increased glucose consumption in IR-HepG2 cells, among which the 500 μM dose produced an improvement comparable to that of the positive control, metformin.

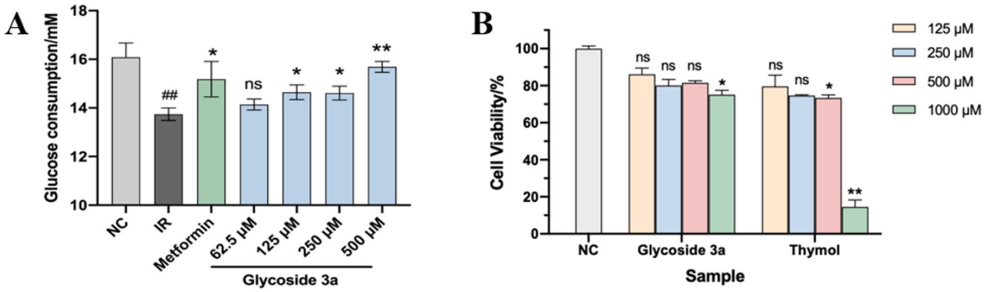


Figure 8. (**A**)The effect of A on the glucose consumption of IR-HepG2 cells. (**B**) Effects of glycoside **3a** on THLE-2 cells. (Note: vs. NC: ## < 0.01; vs. IR: ns > 0.05, 0.01 < * p < 0.05, ** p < 0.01).

2.6.2. Cell Cytotoxicity

To evaluate and compare the cytotoxic effects of glycoside **3a–c** and its natural counterpart phenols on normal human cells, cell viability was assessed using the MTT assay in THLE-2 cells exposed to varying concentrations of the compounds to be tested [38]. The results (Figure 8B and Figure S12) showed that glycoside **3a–c** exhibited superior hepatocyte safety compared to their corresponding natural phenols. At a concentration of 1000 μM, the cell viability of the vanillic acid group decreased to 14.5%, indicating marked cytotoxicity. In contrast, glycoside **3a** exhibited no significant cytotoxicity, maintaining cell viability above 75% at the same concentration, thereby demonstrating a markedly improved safety profile relative to thymol.

3. Discussion

Previous studies have established that glucoside conjugates represent a significant class of α-glucosidase inhibitors, with numerous high-potency derivatives reported to date [39,40]. However, NAG, a critical bioactive derivative of glucose, remains relatively underexplored in this context. In the present study, three phenolic NAG glycosides were synthesized utilizing readily accessible glycosyl chloride and simplified phenolic aglycones. Preliminary bioassays confirmed that all synthesized conjugates possessed α-glucosidase inhibitory activity. Among the tested compounds, glycoside **3a** containing a thymol moiety showed the highest inhibitory activity, approaching that of the reference inhibitor acarbose.

Regarding the underlying mechanism, molecular docking simulations indicated that compound **3a** possesses a lower binding energy and a more extensive network of hydrogen bond interactions compared to its counterparts. Further analysis suggests that the electronic properties and structural polarity distribution between the NAG scaffold and the thymol group enhance its affinity for the enzymE′s catalytic center. Interesting, docking results revealed a dual-site binding mode: glycoside **3a** interacts not only with the active site of the apo-enzyme but also with the product release channel of the substrate-enzyme complex. This observation is consistent with the characteristics of a typical mixed-type inhibitor, a finding further corroborated by our enzyme kinetics data.

In contrast to conventional inhibitors that typically induce protein compaction and rigidification, the binding of glycoside **3a** to the α-glucosidase active site significantly increased the flexibility of several key amino acid residues. This resulted in an expansion of the protein's radius of Rg and SASA. The observed structural destabilization and conformational disorder likely interfere with the enzymE′s native catalytic architecture, resulting in reduced enzymatic activity.

Furthermore, evaluations within an insulin-resistant cell model demonstrated that glycoside **3a** significantly ameliorated impaired glucose metabolism, highlighting its potent anti-diabetic efficacy. The low cytotoxicity observed in our assays further underscores the therapeutic potential and safety profile of NAG glycosides in diabetes management. Given

that the aglycones employed in this study were limited to structurally simple phenols, further optimization through the incorporation of more complex and bioactive marine-derived scaffolds, such as selected flavonoids or terpenoids, may represent a feasible approach to enhance inhibitory potency. Collectively, these findings indicate that NAG-based glycosides constitute a promising scaffold for the development of α-glucosidase inhibitors.

4. Materials and Methods

4.1. Materials

All chemical reagents were employed as received without further purification for the synthesis of the target compounds. NAG, natural phenols and deuterated dimethyl sulfoxide (DMSO-d_6) were purchased from Shanghai Aladdin Biochemical Technology Co., Ltd. (Shanghai, China). Reaction progress was monitored by thin-layer chromatography (TLC) on pre-coated silica gel plates, with visualization under ultraviolet (UV) light at 254 nm. Nuclear magnetic resonance (NMR) spectra of the glycoside conjugates were recorded on a Bruker 600 MHz spectrometer. DMSO-d_6 served as the solvent, and tetramethylsilane (TMS) was used as the internal standard (δ = 0 ppm). Melting points were determined using the SGW®X-4 microscope (manufactured by Shanghai INESA Physico-Optical Instrument Co., Ltd., Shanghai, China). High-resolution mass spectrometry (HRMS) was employed to determine the molecular masses of the compounds by the LTQ Orbitap XL instrument (Thermo Fisher, Bremen, Germany). α-Glucosidase, p-Nitrophenyl-α-D-glucopyranoside (α-PNPG), acarbose and dimethyl sulfoxide (DMSO) were purchased by Yuanye (Shanghai, China). MTT and phosphate-buffered saline (PBS) were purchased by Solarbio (Beijing, China). DMEM medium, fetal bovine serum, penicillin and streptomycin were purchased by Gibco Life Technologies (New York, NY, USA).

4.2. General Procedure for the Preparation of Phenolic Glycosides **3a–c**

4.2.1. Synthesis of the Intermediate 1

According to the method described in the work, intermediate 1 can be obtained efficiently [41].

4.2.2. General Synthesis of the Phenolic Glycosides 3

Intermediate **1** (1 mmol), the phenolic substrate (2 mmol), and anhydrous potassium carbonate (2 mmol) were suspended in acetonitrile (10 mL) containing 1% polyethylene glycol 400 (PEG-400). The mixture was stirred vigorously at room temperature for 12 h. Upon completion, the reaction mixture was filtered to remove insoluble solids. The filtrate was concentrated under reduced pressure. The resulting residue was dissolved in ethyl acetate (10 mL), and the organic phase was sequentially washed with water, saturated aqueous sodium bicarbonate, and saturated brine. The organic layer was dried over anhydrous magnesium sulfate, filtered, and concentrated under reduced pressure. The crude product was purified by flash column chromatography on silica gel using a mixture of dichloromethane (DCM) and methanol (50:1, v/v) as the eluent.

Compound **2** (2 mmol) and sodium methoxide (1 mmol) were dissolved in methanol (10 mL). The reaction mixture was stirred at room temperature for 1–2 h, with progress monitored by TLC. After completion, the reaction was quenched by adding IR-120+ cationic resin and stirring until neutralization was achieved. The resin was removed by filtration, and the filtrate was concentrated under reduced pressure. The residue was dissolved in a minimal volume of a 1:1 (v/v) mixture of MeOH and DCM. This solution was added dropwise to anhydrous diethyl ether. The mixture was allowed to stand at 4 °C overnight. The precipitated solid was collected by filtration and washed with ice-cold anhydrous diethyl ether to afford pure phenolic glycosides **3**.

N-((2S,3R,4R,5S,6R)-4,5-Dihydroxy-6-(hydroxymethyl)-2-(2-isopropyl-5-methylphenoxy) tetrahydro-2H-pyran-3-yl) Acetamide (**3a**)

Glycoside **3a** is white solid, yield: 51.2%. MP: 196.1~198.1 °C. ^{1}H NMR (600 MHz, DMSO-d6) δ 7.79 (d, *J* = 9.3 Hz, 1H), 7.05 (d, *J* = 7.7 Hz, 1H), 6.89 (d, *J* = 1.7 Hz, 1H), 6.77 (dd, *J* = 7.9, 1.6 Hz, 1H), 5.11 (d, *J* = 5.3 Hz, 1H), 5.05 (d, *J* = 5.4 Hz, 1H), 4.82 (d, *J* = 8.5 Hz, 1H), 4.64 (t, *J* = 5.8 Hz, 1H), 3.81 − 3.72 (m, 2H), 3.50 (dt, *J* = 12.1, 6.2 Hz, 1H), 3.40 − 3.34 (m, 1H), 3.30 (ddd, *J* = 9.8, 6.0, 2.0 Hz, 1H), 3.24 − 3.14 (m, 2H), 2.23 (s, 3H), 1.79 (s, 3H), 1.07 (dd, *J* = 11.4, 6.9 Hz, 6H). ^{13}C NMR (151 MHz, DMSO) δ 169.48 (s), 155.02 (s), 136.25 (s), 134.34 (s), 125.95 (s), 122.92 (s), 115.80 (s), 100.21 (s), 77.72 (s), 75.35 (s), 74.71 (s), 70.86 (s), 70.66 (s), 61.26 (s), 55.70 (s), 25.83 (s), 23.59 (s), 23.52 (s), 23.17 (s), 21.45 (s), 21.30 (s). HRMS (-ESI): calcd for C18H27NO6 [M-H]$^{-}$ 352.17656, found 352.17670.

N-((2S,3R,4R,5S,6R)-2-(4-Allyl-2-methoxyphenoxy)-4,5-dihydroxy-6-(hydroxymethyl) tetrahydro-2H-pyran-3-yl) Acetamide (**3b**)

Glycoside **3b** is white solid, yield: 52.8%. MP: 197.8~199.8 °C. ^{1}H NMR (600 MHz, DMSO-d6) δ 7.79 (d, *J* = 9.0 Hz, 1H), 7.03 (d, *J* = 8.2 Hz, 1H), 6.79 (d, *J* = 2.0 Hz, 1H), 6.68 (dd, *J* = 8.3, 2.0 Hz, 1H), 5.93 (ddt, *J* = 16.8, 9.8, 6.7 Hz, 1H), 5.22 − 5.19 (m, 1H), 5.16 (s, 1H), 5.08 (dt, *J* = 17.0, 1.8 Hz, 1H), 5.03 (dd, *J* = 10.0, 1.9 Hz, 1H), 4.94 − 4.86 (m, 1H), 4.62 (d, *J* = 5.8 Hz, 1H), 3.71 (s, 3H), 3.69 (s, 1H), 3.65 − 3.55 (m, 1H), 3.53 −3.42 (m, 2H), 3.41 (d, *J* = 9.7 Hz, 1H), 3.29 (d, *J* = 6.7 Hz, 2H), 3.24 − 3.13 (m, 2H), 1.83 (s, 1H), 1.80 (s, 3H). ^{13}C NMR (151 MHz, DMSO) δ 169.63 (s), 149.95 (s), 145.96 (s), 138.32 (s), 134.80 (s), 121.03 (s), 117.75 (s), 116.06 (s), 114.22 (s), 100.62 (s), 91.05 (s), 77.77 (s), 74.47 (s), 72.54 (s), 71.65 (s), 70.87 (s), 61.62 (s), 61.26 (s), 56.59 (s), 56.18 (s), 54.80 (s), 40.51 (s), 40.39 (s), 40.25 (s), 40.12 (s), 39.98 (s), 39.84 (s), 39.70 (s), 39.56 (s), 39.54 (s), 23.57 (s), 23.15 (s). HRMS (-ESI): calcd for C18H25NO7 [M-H]$^{-}$ 366.15582, found 366.15558.

N-((2S,3R,4R,5S,6R)-4,5-Dihydroxy-6-(hydroxymethyl)-2-(5-isopropyl-2-methylphenoxy) tetrahydro-2H-pyran-3-yl) Acetamide (**3c**)

Glycoside **3c** is white solid, yield: 56.1%. MP: 193.8~195.8 °C. ^{1}H NMR (600 MHz, DMSO-d6) δ 8.50 (s, 1H), 7.81 (d, *J* = 9.2 Hz, 1H), 7.01 (d, *J* = 7.6 Hz, 1H), 6.96 (d, *J* = 1.7 Hz, 1H), 6.76 (dd, *J* = 7.7, 1.7 Hz, 1H), 5.28 (s, 1H), 5.24 (s, 1H), 4.77 (d, *J* = 8.5 Hz, 1H), 4.70 (t, *J* = 5.8 Hz, 1H), 3.81 − 3.72 (m, 2H), 3.49 (dt, *J* = 10.9, 4.9 Hz, 1H), 3.38 (t, *J* = 9.4 Hz, 1H), 3.29 (ddd, *J* = 8.7, 6.4, 2.1 Hz, 1H), 3.18 (t, *J* = 9.2 Hz, 1H), 2.80 (hept, *J* = 7.0 Hz, 1H), 2.03 (s, 3H), 1.81 (s, 3H), 1.17 (d, *J* = 6.9 Hz, 6H). ^{13}C NMR (151 MHz, DMSO) δ 169.53 (s), 156.42 (s), 147.89 (s), 130.44 (s), 124.20 (s), 120.07 (s), 113.23 (s), 100.78 (s), 100.25 (s), 77.90 (s), 74.64 (s), 71.02 (s), 61.30 (s), 61.15 (s), 60.52 (s), 55.69 (s), 33.74 (s), 24.41 (s), 24.32 (s), 23.56 (s), 16.10 (s), 15.67 (s). HRMS (-ESI): calcd for C18H27NO6 [M-H]$^{-}$ 352.17656, found 352.17676.

4.3. α-Glucosidase Inhibitory Activity Assay

The enzyme inhibition assay was performed according to previous reports with minor modifications [8,42]. The experimental design included a blank control group, a no-sample control group, a positive control (acarbose), and experimental groups (samples at various concentrations), with three replicate wells per group. In each well of a 96-well plate, 40 μL of PBS or PBS-dissolved sample solution and 10 μL of α-glucosidase (0.5 U/mL) were added. After incubation at 37 °C for 10 min, 1 mM p-nitrophenyl-α-D-glucopyranoside (pNPG) was introduced, followed by incubation at 37 °C for 30 min. The absorbance at 405 nm was then measured using a multifunctional microplate reader. Nonlinear fitting analysis of compound inhibition rates was performed using GraphPad Prism 9, and the half-maximal inhibitory concentration (IC_{50}) of the compounds was calculated. The percentage of inhibition was calculated using the following equation:

$$\text{Inhibition rate (\%)} = [1 - (\text{Abs experimental} - \text{Abs blank})/(\text{Abs no-sample} - \text{Abs blank})] \times 100\%$$

4.4. Quantum Chemical Calculations

The structures of the phenolic glycosides were constructed using GaussView 5.0 and subsequently optimized by DFT at the B3LYP/6-311G(d,p) level. All calculations were performed with Gaussian 09, and the molecular images were generated using GaussView 5.0.

4.5. Molecular Docking

As the crystal structure of P53341 is unavailable, its predicted structure generated by AlphaFold3 (AF3) was employed (https://alphafold.ebi.ac.uk/, accessed on 10 June 2025). The three-dimensional structure of glycosides and phenols was constructed using Chem3D 20 and subsequently energy-minimized using the built-in molecular mechanics optimization module. Protein and ligand preparation, including the addition of polar hydrogens and assignment of Gasteiger charges, was conducted using AutoDockTools v1.5.7. Molecular docking simulations were then executed using AutoDock Vina v1.2.7 [43]. A blind docking approach was adopted, necessitating a grid box large enough to encompass the entire protein structure. The grid dimensions were set to X = 48.89 Å, Y = 39.11 Å, and Z = 41.07 Å, with a grid point spacing of 1.0 Å. The center of the grid box was positioned at coordinates X = 17.70, Y = 0.18, Z = 17.06. Following successful completion of the docking calculations, the predicted binding affinity (expressed as ΔG in kcal/mol) was obtained. The docking pose exhibiting the most favorable binding energy was selected as the most stable conformation and visualized using PyMOL v3.1.0 software.

4.6. Mechanism of Enzyme Inhibition by Glycoside **3a**

4.6.1. Enzyme Kinetics Assay

Varying concentrations of glycoside **3a** (0, 125, 250, and 500 μM) and α-glucosidase (0.5 U/mL) were added to a 96-well plate and incubated at 37 °C for 10 min. Subsequently, different concentrations of the substrate pNPG (0.5, 1, 2, 4, and 8 mM) were introduced and incubated at 37 °C for 30 min. Absorbance was measured at 405 nm, and kinetic parameters were analyzed by Lineweaver–Burk plots using GraphPad Prism 9.

4.6.2. CD Spectra

CD spectral scanning was performed according to previous reported methods [44,45]. Glycoside **3a** at different concentrations (0, 200, and 400 μM) was mixed with α-glucosidase solution and incubated at room temperature for 20 min. The samples were then scanned in the far-ultraviolet region (190–250 nm) using a CD spectrometer, with each measurement performed in triplicate.

4.7. Molecular Dynamics

To elucidate the specific amino acid residues mediating the interaction between glycoside **3a** and α-glucosidase, MD simulations of the protein-ligand complex were performed using GROMACS 2024.5 [46]. The glycoside **3a** was first optimized at the B3LYP/6-31G(d,p) level and subjected to single-point energy calculation at the M062X/6-311+G(d,p) level using Gaussian 09. Atomic partial charges for **3a**, derived from the M062X/6-311+G(d,p) electrostatic potential via Multiwfn, along with General AMBER Force Field (GAFF) parameters generated by Sobtop, were used to create its topology [47]. The α-glucosidase topology was generated using the GROMACS pdb2gmx tool. The solvated complex, employing the TIP3P water model within a periodic boundary box, was neutralized with Na^+ and Cl^- ions and energy-minimized using the conjugate gradient algorithms until convergence.

Subsequently, the system underwent 100 ps of NPT equilibration at 298.15 K using the V-rescale thermostat and 1 bar using the Berendsen barostat to achieve uniform density. Finally, a 200 ns production MD simulation was conducted under NPT conditions using the same thermostats/barostat. Bond lengths were constrained with LINCS, long-range electrostatics were treated with PME (grid spacing 1.0 Å, real-space cutoff 1.0 nm), and van der Waals interactions were truncated at 1.0 nm. A 2 fs integration time step was used, with coordinates and energies saved every 10 ps for subsequent analysis.

4.8. Glucose Consumption Assay in Insulin-Resistant HepG2 Cells

HepG2 cells in the logarithmic growth phase were seeded into 96-well plates at a density of 1×10^4 cells per well and incubated for 24 h at 37 °C in a humidified atmosphere containing 5% CO_2. Four experimental groups were established: the normal control (NC), the insulin-resistant model (IR), the positive control (metformin), and the glycoside **3a** treatment group. Except for the NC group, all other groups were exposed to 18 mM glucosamine for 20 h to induce insulin resistance. After induction, the culture medium of the NC and IR groups was replaced with fresh complete medium, whereas the positive control and treatment groups were supplied with medium containing metformin (1 mM) or glycoside **3a**, respectively, and further incubated for 24 h. At the end of the treatment, the supernatants were collected, and glucose concentrations were determined using a commercial glucose assay kit following the manufacturer's instructions. Glucose consumption was calculated as the difference between the initial glucose concentration and the residual glucose concentration in the supernatant of each well.

4.9. Cytotoxicity

THLE-2 cells in the logarithmic growth phase were seeded into 96-well plates at a density of 8000 cells per well and cultured in a CO_2 incubator at 37 °C with 5% CO_2 for 24 h. The culture medium was then replaced with 100 μL of fresh medium containing the test compounds at varying concentrations, followed by incubation for an additional 24 h. After treatment, the supernatant was removed, and 100 μL of medium containing MTT (0.5 mg/mL) was added to each well. Following incubation in the dark for 4 h, the medium was replaced with DMSO (150 μL), and the plates were shaken for 10 min to fully dissolve the formazan crystals. Absorbance was measured at 490 nm using a multifunctional microplate reader, and cell viability was calculated according to the following equation:

$$\text{Cell viability (\%)} = \text{Abs sample}/\text{Abs blank} \times 100\% \quad (1)$$

5. Conclusions

In summary, three structurally simple natural phenols were glycosylated with NAG, yielding NAG glycosides that exhibited markedly enhanced α-glucosidase inhibitory activity relative to the corresponding aglycones. Among them, the thymol-derived glycoside **3a** displayed the highest inhibitory potency, comparable to that of acarbose. Cell-based assays further demonstrated favorable cytocompatibility of **3a** and its ability to ameliorate insulin resistance–related glucose metabolism, supporting its potential as a hit compound. Importantly, this study highlights phenolic NAG glycosides as a promising new scaffold for α-glucosidase inhibitor development, presenting a novel approach for the design of glycoside-based therapeutics for diabetes.

Supplementary Materials: The following supporting information can be downloaded at: https://www.mdpi.com/article/10.3390/md24020084/s1, Figure S1: The 1H NMR spectrum of the glycoside 3a; Figure S2: The 13C NMR spectrum of the glycoside 3a; Figure S3: The HRMS of the glycoside 3a; Figure S4: The 1H NMR spectrum of the glycoside 3b; Figure S5: The 13C NMR spectrum of the glycoside 3b; Figure S6: The HRMS of the glycoside 3b; Figure S7: The 1H NMR spectrum of the glycoside 3c; Figure S8: The 13C NMR spectrum of the glycoside 3c; Figure S9: The HRMS of the glycoside 3c; Figure S10: Infrared spectroscopy of glycoside 3a–c; Figure S11: (A) The probability of different RMSD values occurring during the simulation process. (B) The probability of different area values during the simulation process; Figure S12: Effects of glycoside 3b–c on THLE-2 cells; Table S1: The binding energy of glycosides and phenols.

Author Contributions: Conceptualization, R.X.; methodology, W.W. and K.G.; software, K.G.; validation, K.G., G.L., K.L., S.L. and Z.W.; formal analysis, W.W.; investigation, S.L. and H.Y.; resources, K.G.; data curation, W.W.; writing—original draft preparation, W.W.; writing—review and editing, G.L.; supervision, Z.W. and K.L.; project administration, Z.W. and R.X.; funding acquisition, R.X. All authors have read and agreed to the published version of the manuscript.

Funding: This work was supported by The Key R&D Program (Major Scientific and Technological Innovation Project) of Shandong Province, China (2022CXGC020413); the Taishan Industrial Experts Program; the National Natural Science Foundation of China (42276097, 42406119); Qingdao Natural Science Foundation (25-1-1-186-zyyd-jch); Modern Agro-industry Technology Research System (CARS-49); Central guidance for local scientific and technological development funds (2024ZY0039).

Institutional Review Board Statement: Not applicable.

Data Availability Statement: All data included in this work are available upon request.

Acknowledgments: We thank associate researcher Xin Li from our institute for assistance in resolving the licensing issues of Gaussian 09 software.

Conflicts of Interest: The authors declare no conflicts of interest.

References

1. Xiao, D.; Lu, L.; Liang, B.; Xiong, Z.; Xu, X.; Chen, W.-H. Identification of 1,3,4-oxadiazolyl-containing beta-carboline derivatives as novel alpha-glucosidase inhibitors with antidiabetic activity. *Eur. J. Med. Chem.* **2023**, *261*, 115795. [PubMed]
2. Kushawaha, A.K.; Jaiswal, A.K.; Kumar, P.; Katiyar, S.; Baghel, R.; Bhatt, H.; Gupta, J.; Ansari, A.; Yadav, P.; Ahmad, I.; et al. Development of Novel Phthalazinone-Triazole Hybrids as Potential Antidiabetic Agents Targeting GLUT4 Translocation in Skeletal Muscle. *J. Med. Chem.* **2025**, *68*, 10722–10737. [CrossRef] [PubMed]
3. Martiniakova, M.; Sarocka, A.; Penzes, N.; Biro, R.; Kovacova, V.; Mondockova, V.; Sevcikova, A.; Ciernikova, S.; Omelka, R. Protective Role of Dietary Polyphenols in the Management and Treatment of Type 2 Diabetes Mellitus. *Nutrients* **2025**, *17*, 275. [CrossRef] [PubMed]
4. Ding, X.-M.; Zhang, X.; Wei, X.-Y.; Wu, R.-Q.; Gu, Q.; Zhou, T. Hypoglycemic and Gut Microbiota-Modulating Effects of Pectin from *Citrus aurantium* "Changshanhuyou" Residue in Type 2 Diabetes Mellitus Mice. *J. Agric. Food Chem.* **2025**, *73*, 9088–9102. [CrossRef]
5. Ghasemi, M.; Mahdavi, M.; Dehghan, M.; Eftekharian, M.; Mojtabavi, S.; Faramarzi, M.A.; Iraji, A.; Al-Harrasi, A. Substituted piperazine conjugated to quinoline-thiosemicarbazide as potent alpha-glucosidase inhibitors to target hyperglycemia. *Sci. Rep.* **2025**, *15*, 1871.
6. Tokalı, F.S.; Demir, Y.; Ateşoğlu, Ş.; Tokalı, P.; Şenol, H. Development of phenolic Mannich bases as alpha-glucosidase and aldose reductase inhibitors: In vitro and in silico approaches for managing diabetes mellitus and its complications. *Bioorgan. Med. Chem.* **2025**, *128*, 118264. [CrossRef]
7. Yang, W.; Chen, J.; Peng, Z.; Wang, G. Design, synthesis and enzymatic inhibition evaluation of novel 4-hydroxy Pd-C-III derivatives as alpha-glucosidase and PTP1B dual-target inhibitors. *Eur. J. Med. Chem.* **2024**, *280*, 116938. [CrossRef]
8. Liang, B.; Xiao, D.; Wang, S.-H.; Xu, X. Novel thiosemicarbazide-based beta-carboline derivatives as alpha-glucosidase inhibitors: Synthesis and biological evaluation. *Eur. J. Med. Chem.* **2024**, *275*, 116595. [CrossRef]
9. Chen, Y.; Liu, Y.; Chen, N.; Jin, Y.; Yang, R.; Yao, H.; Kong, D.-X. A chemoinformatic analysis on natural glycosides with respect to biological origin and structural class. *Nat. Prod. Rep.* **2023**, *40*, 1464–1478. [CrossRef]

10. Wang, Y.; Yang, J.; Jiang, X.; Yuan, R.; Cheng, R.; Lu, N.; Gao, A.; Liu, S. Potential new drug sources for the treatment of Parkinson's disease: Flavonoid O-glycosides. *Mol. Biol. Rep.* **2025**, *52*, 966. [CrossRef]
11. Chen, D.; Song, Z.; Han, J.; Liu, J.; Liu, H.; Dai, J. Targeted Discovery of Glycosylated Natural Products by Tailoring Enzyme-Guided Genome Mining and MS-Based Metabolome Analysis. *J. Am. Chem. Soc.* **2024**, *146*, 9614–9622. [CrossRef] [PubMed]
12. Feng, J.; He, F.; Huang, Y.; Zhou, M.; Liu, X.; Ye, X.; Yang, R.; Tian, W.; Chen, H. Inhibitory effects of phenolic glycosides from Trollius chinensis Bunge on alpha-glucosidase: Inhibition kinetics and mechanisms. *Food Funct.* **2022**, *13*, 2857–2864. [CrossRef] [PubMed]
13. Zhou, H.; Yang, M.; Chen, J.; Tang, Y.; Shao, J.; Wang, Z.; Zhao, C. Phenolic Glycosides from *Viburnum chinshanense* Leaves and their alpha-Amylase and alpha-Glucosidase Inhibitory Activity. *Chem. Biodivers.* **2024**, *21*, e202400236. [CrossRef] [PubMed]
14. Yuan, L.-L.; Wang, Y.; Wang, G.-K.; Liu, J.-K. Nine New Glycosylated Compounds from the Leaves of the Medicinal Plant *Malus hupehensis*. *Molecules* **2024**, *29*, 5269. [CrossRef]
15. Guo, F.; An, J.; Wang, M.; Zhang, W.; Chen, C.; Mao, X.; Liu, S.; Wang, P.; Ren, F. Inhibitory Mechanism of Quercimeritrin as a Novel alpha-Glucosidase Selective Inhibitor. *Foods* **2023**, *12*, 3415. [CrossRef]
16. Park, M.J.; Kang, Y.-H. Isolation of Isocoumarins and Flavonoids as alpha-Glucosidase Inhibitors from *Agrimonia pilosa* L. *Molecules* **2020**, *25*, 2572.
17. Crawford, C.J.; Seeberger, P.H. Seeberger, Advances in glycoside and oligosaccharide synthesis. *Chem. Soc. Rev.* **2023**, *52*, 7773–7801. [CrossRef]
18. Andreana, P.R.; Crich, D. Guidelines for O-Glycoside Formation from First Principles. *ACS Central Sci.* **2021**, *7*, 1454–1462. [CrossRef]
19. Xie, L.; Deng, Z.; Zhang, J.; Dong, H.; Wang, W.; Xing, B.; Liu, X. Comparison of Flavonoid O-Glycoside, C-Glycoside and Their Aglycones on Antioxidant Capacity and Metabolism During In Vitro Digestion and In Vivo. *Foods* **2022**, *11*, 882. [CrossRef]
20. Peña-Vázquez, G.I.; Dominguez-Fernández, M.T.; Camacho-Zamora, B.D.; Hernandez-Salazar, M.; Urías-Orona, V.; De Peña, M.-P.; de la Garza, A.L. In vitro simulated gastrointestinal digestion impacts bioaccessibility and bioactivity of Sweet orange (*Citrus sinensis*) phenolic compounds. *J. Funct. Foods* **2022**, *88*, 104891. [CrossRef]
21. Alshamari, A.K.; Aboulthana, W.M.; Mansour, H.; Abu-Zied, K.M.; Alshammari, O.A.O.; Morsy, N.M.; Alsaif, N.O.S.; Alshammari, M.Z.; Nossier, E.S.; Hassan, N.A. In Vitro Evaluation of Sugar-Conjugated Thienopyrimidinone Derivatives with Possible Neuroprotective and Antioxidant Effects. *Int. J. Mol. Sci.* **2025**, *26*, 10826. [CrossRef]
22. Cao, S.; Liu, Y.; Shi, L.; Zhu, W.; Wang, H. N-Acetylglucosamine as a platform chemical produced from renewable resources: Opportunity, challenge, and future prospects. *Green Chem.* **2022**, *24*, 493–509. [CrossRef]
23. Gao, K.; Qin, Y.; Liu, S.; Wang, L.; Xing, R.; Yu, H.; Chen, X.; Li, P. A review of the preparation, derivatization and functions of glucosamine and N-acetyl-glucosamine from chitin. *Carbohydr. Polym. Technol. Appl.* **2023**, *5*, 100296. [CrossRef]
24. He, M.; Zhai, Y.; Zhang, Y.; Xu, S.; Yu, S.; Wei, Y.; Xiao, H.; Song, Y. Inhibition of alpha-glucosidase by trilobatin and its mechanism: Kinetics, interaction mechanism and molecular docking. *Food Funct.* **2022**, *13*, 857–866. [CrossRef] [PubMed]
25. He, H.; Lu, Y.-H. Comparison of inhibitory activities and mechanisms of five mulberry plant bioactive components against alpha-glucosidase. *J. Agric. Food Chem.* **2013**, *61*, 8110–8119. [CrossRef] [PubMed]
26. Li, J.; Hu, H.; Chen, X.; Zhu, H.; Zhang, W.; Tai, Z.; Yu, X.; He, Q. A novel ACE inhibitory peptide from Douchi hydrolysate: Stability, inhibition mechanism, and antihypertensive potential in spontaneously hypertensive rats. *Food Chem.* **2024**, *460*, 140734. [CrossRef] [PubMed]
27. Chagas, R.S.; Marana, S.R. Tris inhibits a GH1 beta-glucosidase by a linear mixed inhibition mechanism. *PLoS ONE* **2025**, *20*, e0320120. [CrossRef]
28. Wärmländer, S.K.; Lakela, A.L.; Berntsson, E.; Jarvet, J.; Gräslund, A. Secondary Structures of Human Calcitonin at Different Temperatures and in Different Membrane-Mimicking Environments, Characterized by Circular Dichroism (CD) Spectroscopy. *ACS Omega* **2025**, *10*, 17133–17142. [CrossRef]
29. Dai, T.; Chen, J.; McClements, D.J.; Li, T.; Liu, C. Investigation the interaction between procyanidin dimer and alpha-glucosidase: Spectroscopic analyses and molecular docking simulation. *Int. J. Biol. Macromol.* **2019**, *130*, 315–322. [CrossRef]
30. Pradhan, T.; Gupta, O.; Chawla, G. Identification of novel thiazolidine-4-one based hits as potential PPARγ modulators through in silico workflow and validation through in vitro studies. *J. Mol. Struct.* **2025**, *1339*, 142391. [CrossRef]
31. Ma, Y.; Sun, J.; Xiao, B.-L. A study of the mechanism of α-glucosidase inhibition by rapeseed polyphenols. *LWT* **2025**, *223*, 117716. [CrossRef]
32. Trezza, A.; Visibelli, A.; Roncaglia, B.; Barletta, R.; Iannielli, S.; Mahboob, L.; Spiga, O.; Santucci, A. Unveiling Dynamic Hotspots in Protein-Ligand Binding: Accelerating Target and Drug Discovery Approaches. *Int. J. Mol. Sci.* **2025**, *26*, 3971. [PubMed]
33. Varadharajan, V.; Balu, A.K.; Sinclair, B.J.; Perinbarajan, G.K.; Jenifer A, D.; Sudha, H.G.; Ramaswamy, A.; Venkidasamy, B.; Thiruvengadam, M. Comprehensive analysis of *Syzygium cumini* L. pomace extract as an alpha-amylase inhibitor: In vitro inhibition, kinetics, and computational studies. *Bioorganic Chem.* **2025**, *161*, 108498.

34. Ravi, A.; Zaib, S.; Zahra, S.; Khan, I.; Ali, H.S.; El-Gamal, M.I.; Anbar, H.S. Synthesis, in vitro and in vivo evaluation, and computational modeling analysis of thioxothiazolidine derivatives as highly potent and selective alpha-amylase inhibitors. *Eur. J. Med. Chem.* **2025**, *291*, 117584. [CrossRef] [PubMed]
35. Chen, X.; Zhang, W.; Pan, Y.; Ran, J.; Liu, X.; Yu, X.; He, Q. Preparation, identification, and molecular mechanism of novel DPP-IV inhibitory peptides from pumpkin seed: In silico screening and experimental validation. *Food Chem.* **2025**, *486*, 144530. [CrossRef]
36. Alharbi, A.S.; Altwaim, S.A.; El-Daly, M.M.; Hassan, A.M.; Al-Zahrani, I.A.; Bajrai, L.H.; Alsaady, I.M.; Dwivedi, V.D.; Azhar, E.I. Marine fungal diversity unlocks potent antivirals against monkeypox through methyltransferase inhibition revealed by molecular dynamics and free energy landscape. *BMC Chem.* **2024**, *18*, 141. [CrossRef]
37. Abouzied, A.S.; Alqarni, S.; Younes, K.M.; Alanazi, S.M.; Alrsheed, D.M.; Alhathal, R.K.; Huwaimel, B.; Elkashlan, A.M. Structural and free energy landscape analysis for the discovery of antiviral compounds targeting the cap-binding domain of influenza polymerase PB2. *Sci. Rep.* **2024**, *14*, 25441. [CrossRef]
38. Boateng, A.O.; Patel, V.B.; Bligh, S.W.A. The Hepatoprotective Properties of Gentiopicroside, Sweroside, and Swertiamarin Against Metabolic Dysfunction-Associated Steatotic Liver Disease (MASLD). *Biomolecules* **2025**, *15*, 726. [CrossRef]
39. Rivero-Barbarroja, G.; Padilla-Pérez, M.C.; Maisonneuve, S.; García-Moreno, M.I.; Tiet, B.; Vocadlo, D.J.; Xie, J.; Fernández, J.M.G.; Mellet, C.O. sp(2)-Iminosugar azobenzene O-glycosides: Light-sensitive glycosidase inhibitors with unprecedented tunability and switching factors. *Bioorganic Chem.* **2024**, *150*, 107555. [CrossRef]
40. Hossain, U.; Das, A.K.; Ghosh, S.; Sil, P.C. An overview on the role of bioactive alpha-glucosidase inhibitors in ameliorating diabetic complications. *Food Chem. Toxicol.* **2020**, *145*, 111738.
41. Gao, K.; Qin, Y.; Wang, L.; Li, X.; Liu, S.; Xing, R.; Yu, H.; Chen, X.; Li, P. Design, Synthesis, and Antifungal Activities of Hymexazol Glycosides Based on a Biomimetic Strategy. *J. Agric. Food Chem.* **2022**, *70*, 9520–9535. [CrossRef]
42. Cai, Y.; Wu, L.; Lin, X.; Hu, X.; Wang, L. Phenolic profiles and screening of potential α-glucosidase inhibitors from *Polygonum aviculare* L. leaves using ultra-filtration combined with HPLC-ESI-qTOF-MS/MS and molecular docking analysis. *Ind. Crop. Prod.* **2020**, *154*, 112673. [CrossRef]
43. Eberhardt, J.; Santos-Martins, D.; Tillack, A.F.; Forli, S. AutoDock Vina 1.2.0: New Docking Methods, Expanded Force Field, and Python Bindings. *J. Chem. Inf. Model.* **2021**, *61*, 3891–3898. [CrossRef]
44. Wu, G.; Mao, R.; Zhang, Y.; Zhu, L.; Karrar, E.; Zhang, H.; Jin, Q.; Wang, X. Study on the interaction mechanism of virgin olive oil polyphenols with mucin and α-amylase. *Food Biosci.* **2022**, *47*, 101673. [CrossRef]
45. Wang, S.; Li, Y.; Huang, D.; Chen, S.; Xia, Y.; Zhu, S. The inhibitory mechanism of chlorogenic acid and its acylated derivatives on alpha-amylase and alpha-glucosidase. *Food Chem.* **2022**, *372*, 131334. [CrossRef]
46. Van Der Spoel, D.; Lindahl, E.; Hess, B.; Groenhof, G.; Mark, A.E.; Berendsen, H.J. GROMACS: Fast, flexible, and free. *J. Comput. Chem.* **2005**, *26*, 1701–1718. [CrossRef]
47. Lu, T. A comprehensive electron wavefunction analysis toolbox for chemists. *Multiwfn. J. Chem. Phys.* **2024**, *161*, 082503. [CrossRef]

Disclaimer/Publisher's Note: The statements, opinions and data contained in all publications are solely those of the individual author(s) and contributor(s) and not of MDPI and/or the editor(s). MDPI and/or the editor(s) disclaim responsibility for any injury to people or property resulting from any ideas, methods, instructions or products referred to in the content.